Journal of Industrial and Engineering Chemistry 20 (2014) 3329–3334

Contents lists available at ScienceDirect

Journal of Industrial and Engineering Chemistry

journal homepage: www.elsevier.com/locate/jiec

Photocatalytic conversion of 4-nitroaniline to p-phenylenediamine using Ni/$ZnSn(OH)_6$ nanoparticles

R.M. Mohamed [a,b,c,*], E.S. Aazam [a]

[a] Department of Chemistry, Faculty of Science, King Abdulaziz University, P.O. Box 80203, Jeddah 21589, Saudi Arabia
[b] Advanced Materials Department, Central Metallurgical R&D Institute, CMRDI, P.O. Box 87, Helwan, Cairo 11421, Egypt
[c] Center of Excellence in Environmental Studies, King Abdulaziz University, P.O. Box 80216, Jeddah 21589, Saudi Arabia

ARTICLE INFO

Article history:
Received 8 November 2013
Accepted 4 December 2013
Available online 12 December 2013

Keywords:
$ZnSn(OH)_6$
Ni doping
Synthesis of p-phenylenediamine
Visible photocatalyst

ABSTRACT

$ZnSn(OH)_6$ nanoparticles were prepared using a hydrothermal method, and Ni was immobilised onto the surface of the $ZnSn(OH)_6$ nanoparticles via a photo-assisted deposition (PAD) method. The samples produced were characterised using different techniques. The catalytic performances of the $ZnSn(OH)_6$ and Ni/$ZnSn(OH)_6$ samples were examined in the photoreduction of 4-nitroaniline to aniline under visible light. The UV–vis spectral analysis detected a red shift after loading the Ni onto the $ZnSn(OH)_6$. The maximum photocatalytic reduction efficiency of 4-nitroaniline that was achieved was 100% after 60 min of reaction time with 0.3 Ni/$ZnSn(OH)_6$ as the photocatalyst.

1. Introduction

Hydrogenation of 4-nitroaniline (4-NA) is an important reaction in the field of chemical industry, since the produced p-phenylenediamine (PPD) is a useful component to many industrial chemicals (e.g., rubber antioxidants, textile fibres and thermoplastics) [1–3]. Generally, the hydrogenation of 4-NA is achieved by using noble metals under H_2 atmosphere [3]. New methods for water treatment and improvements in the existing processes are needed to protect our environment. Heterogeneous photocatalysis, known as Advanced Oxidation Processes (AOPs), has recently gained much attention. The photocatalytic activity of TiO_2 [4–11] was more effective in removing dyes and phenolics from aqueous solutions than conventional techniques such as chemical precipitation, filtration, electro-deposition, ion-exchange adsorption, membrane systems [12] and (AOPs) [13]. Therefore, TiO_2 is by far the most popular method because of its higher photocatalytic activity, good photostability, non-toxicity, and low price. However, effective commercial applications are hindered by two serious disadvantages. The first is the agglomeration of ultrafine powders resulting in an adverse effect on catalyst performance. The second is the large band gap of 3.2 eV, so wavelengths below 400 nm are necessary for excitation, which limits the usage efficiency of solar energy. The large band gap of TiO_2 (3.2 eV) limits its photocatalytic applications to the UV range. UV light is about 4% of the solar spectrum and can be easily filtered with clear glass or pure water. Therefore, it would be useful to modify the band gap of TiO_2 to improve its optical properties. In recent decades, doping with nonmetals has been performed to shift the optical response of the catalytically active TiO_2 from the UV to the visible light region. Mordenite [14], graphene [15,16], F [17], Sm [18], Ni [19], Pt [20], Au [26], Ag [21,22], rare earth dopants [23], and Co, Cr, Ag [24], and Pd [25,26] have been used to extend the photoresponse range of the TiO_2 matrix. Of late, some hydroxide-based photocatalysts (InOOH, $In(OH)_3$) have been explored for the photodegradation of benzene and showed high photoactivities [27,28]. The $CaSnO_3$ obtained from the precursor $CaSn(OH)_6$ also exhibited good performance for methyl orange degradation [29]. In the above photocatalysts, all central metal ions (Sn^{4+}, In^{3+}) possess d^{10} electronic configuration which has been reported to be favourable for the separation of photogenerated electron/hole pairs [30,31]. $ZnSn(OH)_6$ is another hydroxide-based material. The main drawback associated with $ZnSn(OH)_6$ semiconductor photocatalyst is absorption in UV region. Therefore, the main goal of the researchers is to decrease the band gap of $ZnSn(OH)_6$ by Ni doping. To the best of our knowledge, there are no reports of reduction of 4-NA using $ZnSn(OH)_6$. The present study aims in synthesis, characterisation of Ni/$ZnSn(OH)_6$ and evaluation of their photocatalytic activity for the reduction of 4-NA in aqueous phase.

* Corresponding author at: Department of Chemistry, Faculty of Science, King Abdulaziz University, P.O. Box 80203, Jeddah 21589, Saudi Arabia.
Tel.: +966 540715648; fax: +966 26400376.
E-mail address: mhmdouf@gmail.com (R.M. Mohamed).

1226-086X/$ – see front matter © 2013 The Korean Society of Industrial and Engineering Chemistry. Published by Elsevier B.V. All rights reserved.
http://dx.doi.org/10.1016/j.jiec.2013.12.016

2. Experimental

2.1. Preparation of $ZnSn(OH)_6$

All of the reagents were of analytical grade and were used without further purification. The $ZnSn(OH)_6$ nanoparticles were prepared via a hydrothermal method. First, 0.1 M of $ZnCl_2$ and 0.1 M of $SnCl_4{\cdot}5H_2O$ were prepared by dissolving the required amount of each salt in distilled water. Secondly, a 25 mL aliquot of the $ZnCl_2$ solution was slowly added under continuous stirring to 25 mL of the $SnCl_4{\cdot}5H_2O$ solution, and then, the pH of the mixture was adjusted to 12 with ammonia. The resulting mixture was transferred into a 100 mL Teflon-lined autoclave and was maintained at 120 °C for 24 h. After the experimental run, the autoclave was taken out of the hot air oven and was naturally cooled to room temperature. The synthesised material was collected from the Teflon liner and was washed with distilled water three times; then, it was dried for 1 h at 60 °C in a hot air oven to eliminate the moisture content from the final product.

2.2. Preparation of $Ni/ZnSn(OH)_6$

$Ni/ZnSn(OH)_6$ containing 0.1, 0.2, 0.3, and 0.4 wt% of Ni metal were synthesised using the photo-assisted deposition (PAD) route as follows: Ni metal was deposited on $ZnSn(OH)_6$ using an aqueous solution of $Ni(NO_3)_2$ under UV irradiation. The samples were dried at 100 °C, and this was followed by H_2-reduction (20 mL min^{-1}) at 150 °C for 2 h.

2.3. Characterisation techniques

X-ray diffraction (XRD) analysis was carried out at room temperature with a Bruker axis D8 instrument using Cu Kα radiation (λ = 1.540 Å). The specific surface area was calculated from measurements of the N_2 adsorption using a Nova 2000 series Chromatech apparatus at 77 K. Prior to the measurements, all of the samples were treated under a vacuum at 250 °C for 2 h. The band gap for each of the samples was identified by UV–visible diffuse reflectance spectra (UV–vis-DRS). The measurements were taken in air at room temperature over the wavelength range of 200–800 nm using a UV/vis/NIR spectrophotometer (V-570, JASCO, Japan). The transmission electron microscopy (TEM) was recorded with a JEOL-JEM-1230 microscope. The samples were prepared by suspending them in ethanol and then ultrasonicating them for 30 min. Subsequently, a small amount of this solution was put onto a carbon-coated copper grid before it was dried and loaded into the TEM. X-ray photoelectron spectroscopy (XPS) studies were performed using a Thermo Scientific K-ALPHA, XPS, England.

2.4. Photoreaction apparatus and procedure

The photocatalytic apparatus consisted of two parts. The first part was an annular quartz tube. A 500 W Xenon lamp (Institute of Electric Light Source, Beijing) was used as the visible light source. The wavelength of the visible light was controlled by a cut-off filter ($\lambda > 420$ nm). The lamp was laid in an empty chamber of the annular tube, and running water was passed through the inner thimble of the annular tube. Owing to the continuous cooling, the temperature of the reaction solution was maintained at approximately 30 °C. The second part was a sealed quartz reactor, which was located below the lamp. For each photochemical reaction, a photocatalyst sample was ultrasonically dispersed in 80 mL of a 4-NA/CH_3OH solution (1/99, v/v). The initial concentration of 4-NA was 40 ppm. The distance between the light source and the surface of the reaction solution was 11 cm. Nitrogen was passed through the solution for 0.5 h before illumination to remove the dissolved oxygen in the solution to ensure that the photoinduced electrons could be involved in the reduction of 4-NA. As the reaction proceeded, 4 mL of the suspension was taken at a certain interval and was filtrated. The 4-NA and PPD concentrations during the reaction were analysed by measuring the absorbance at 380 and 238 nm with an UV/vis/NIR spectrophotometer (V-570, JASCO, Japan), respectively. The whole photocatalytic process was carried out under N_2 bubbling with a flow rate of 60 mL min^{-1}.

3. Results and discussion

3.1. Structural, morphological, and compositional characterisations

The XRD patterns of the parent $ZnSn(OH)_6$ and $Ni/ZnSn(OH)_6$ nanoparticles are compared in Fig. 1. The structural characteristics of $ZnSn(OH)_6$ and $Ni/ZnSn(OH)_6$ are mainly composed of zinc hydroxystannate (JCPDS Card: 20-1455), which indicated that the $ZnSn(OH)_6$ structure remained conserved after the use of the photo-assisted deposition (PAD) methodology. However, no diffraction peaks indicative of Ni in the patterns of the $Ni/ZnSn(OH)_6$ samples appeared. This can likely be attributed to the low Ni doping content. However, the data may also imply that Ni was well dispersed within the $ZnSn(OH)_6$ phase. Ni played a prominent role in the process of crystallisation as was demonstrated by XRD patterns which showed that the characteristic diffraction peaks of the $ZnSn(OH)_6$ phase became broad, and their intensities decreased with increased Ni loading. The average crystallite sizes of the $ZnSn(OH)_6$ were calculated by Scherer's equation using the full width at the half maximum of the X-ray diffraction peaks at $\theta = 22.92°$, which corresponded to the most intense $ZnSn(OH)_6$ peak. The crystallite sizes of the $ZnSn(OH)_6$, 0.1 wt% $Ni/ZnSn(OH)_6$, 0.2 wt% $Ni/ZnSn(OH)_6$, 0.3 wt% $Ni/ZnSn(OH)_6$ and 0.4 wt% $Ni/ZnSn(OH)_6$ were 22 19, 17, 14, and 11 nm, respectively. Therefore, the particle size became smaller as the nickel concentration increased.

XPS spectres of 0.3 wt% $Ni/ZnSn(OH)_6$ nanocomposites are shown in Fig. 2. The XPS spectra (Fig. 2A–C) demonstrated that Zn; Sn and O species were present, corresponding to binding energy of 1022.25, 1045.47; 486.6, 495 and 531.1 eV correspond to the binding energies of Zn 2p; Sn 3d and O 1 s for $ZnSn(OH)_6$, respectively. The peak observed at 853 and 870 eV was ascribed to metallic nickel (Fig. 2D).

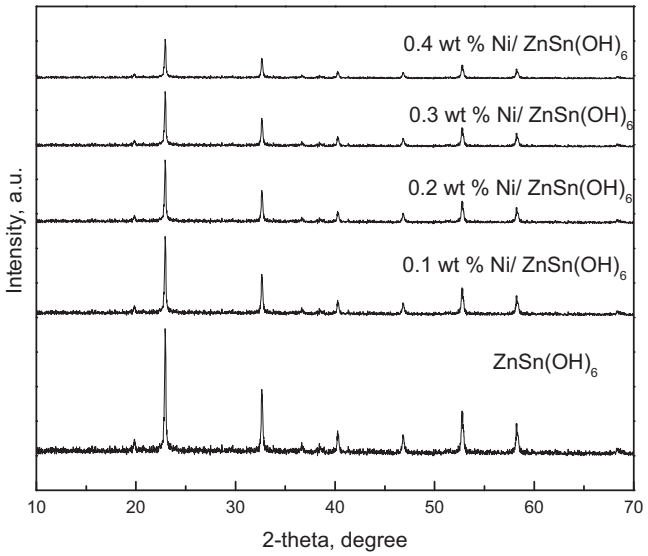

Fig. 1. XRD patterns of $ZnSn(OH)_6$ and $Ni/ZnSn(OH)_6$ nanoparticles.

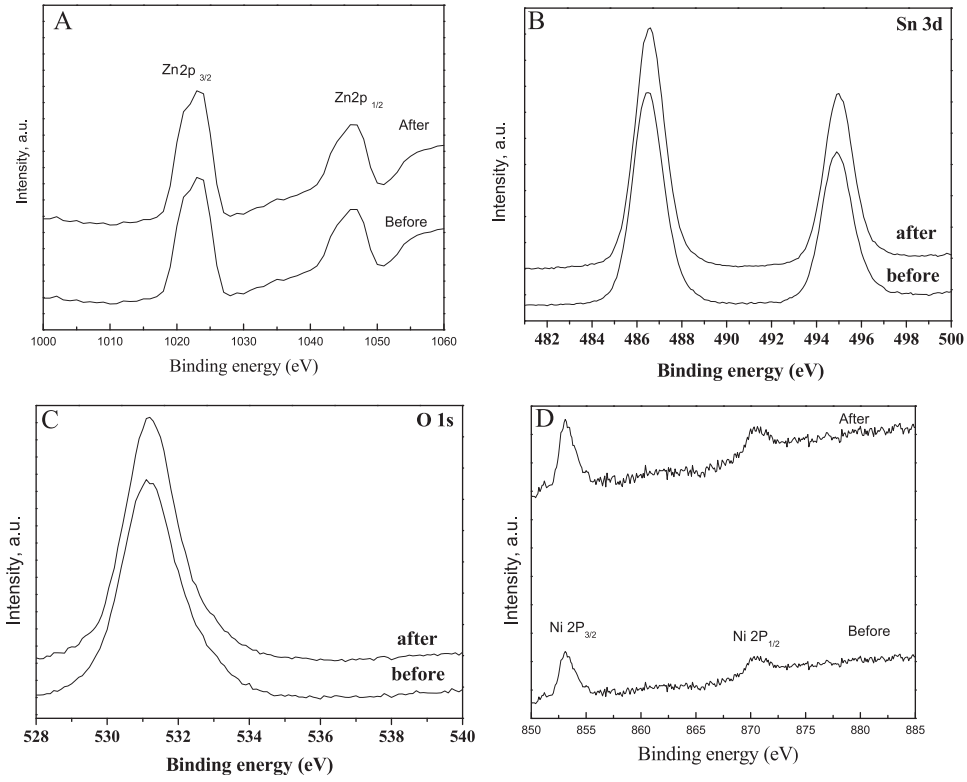

Fig. 2. X-ray photoelectron spectra for 0.3 wt% Ni/$ZnSn(OH)_6$.

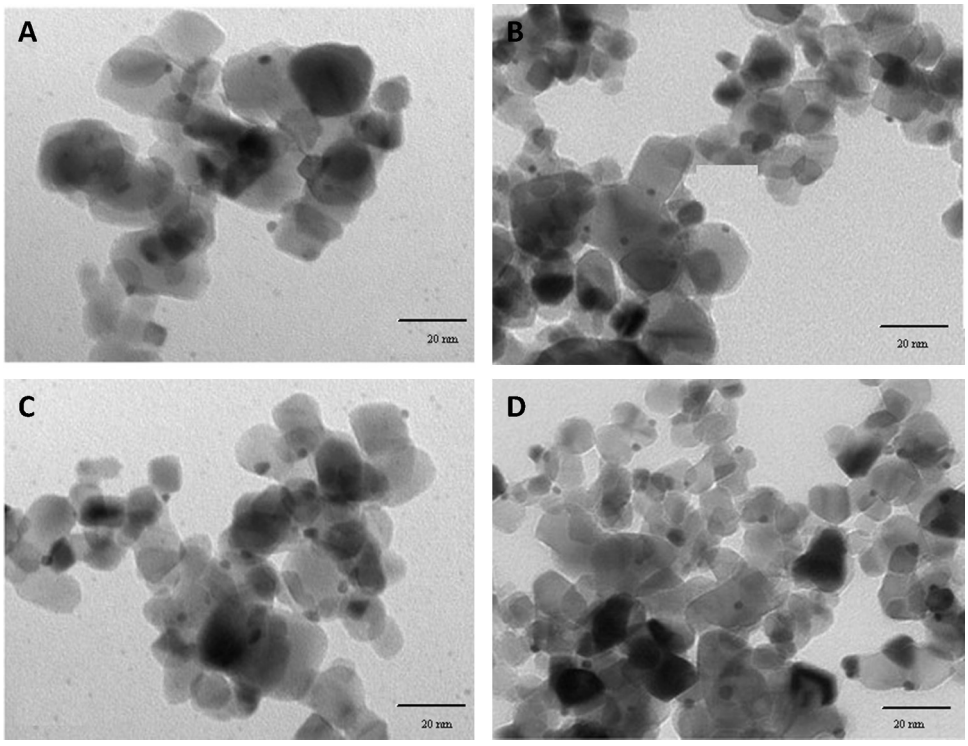

Fig. 3. TEM images of Ni/$ZnSn(OH)_6$ nanoparticles, where the wt% of Ni is 0.1 (A), 0.2 (B), 0.3 (C), and 0.4 (D).

The TEM images of Ni/$ZnSn(OH)_6$ nanoparticles are shown in Fig. 3. The results revealed that the number of Ni ions dispersed on the surface of the catalyst, and the diameter of the Ni ions both increased as the wt% of Ni was increased, and the diameter of the $ZnSn(OH)_6$ decreased as the wt% of Ni was increased. It is clear that the Ni homogeneity also increased as the amount of Ni ions increased up to 0.3 wt%. However, at a higher concentration of Ni ions, i.e., 0.4 wt%, the Ni homogeneity decreased. This observation indicated that there was an optimum value for the deposition of the Ni ions.

Table 1
Texture parameters of $ZnSn(OH)_6$ and $Ni/ZnSn(OH)_6$ nanoparticles.

Sample	S_{BET} (m^2/g)	S_t (m^2/g)	Total V_p (mL/g)	r (Å)
$ZnSn(OH)_6$	90.00	93.00	0.192	41.00
0.1 wt% $Ni/ZnSn(OH)_6$	88.00	89.00	0.188	43.00
0.2 wt% $Ni/ZnSn(OH)_6$	85.00	87.00	0.185	45.00
0.3 wt% $Ni/ZnSn(OH)_6$	83.00	85.00	0.183	52.00
0.4 wt% $Ni/ZnSn(OH)_6$	81.00	83.00	0.180	55.00

S_{BET}, BET surface area.
S_t, surface area derived from V_{l-t} plots.
r, mean pore radius.
V_p, total pore volume.

Table 2
Band gap energy of $ZnSn(OH)_6$ and $Ni/ZnSn(OH)_6$ nanoparticles.

Sample	Band gap energy (eV)
$ZnSn(OH)_6$	3.45
0.1 wt% $Ni/ZnSn(OH)_6$	3.21
0.2 wt% $Ni/ZnSn(OH)_6$	3.03
0.3 wt% $Ni/ZnSn(OH)_6$	2.79
0.4 wt% $Ni/ZnSn(OH)_6$	2.77

3.2. Surface area analysis

Specific surface areas (S_{BET}) of the parent $ZnSn(OH)_6$ and $Ni/ZnSn(OH)_6$ nanoparticles were determined. The S_{BET} values were 90, 88, 85, 83 and 81 m^2/g for the $ZnSn(OH)_6$, 0.1 wt% $Ni/ZnSn(OH)_6$, 0.2 wt% $Ni/ZnSn(OH)_6$, 0.3 wt% $Ni/ZnSn(OH)_6$ and 0.4 wt% $Ni/ZnSn(OH)_6$, respectively. The surface area parameters and the data calculated from the *t*-plot are compiled in Table 1. Furthermore, the total pore volume of the $ZnSn(OH)_6$ was higher than in the $Ni/ZnSn(OH)_6$ samples due to the blockage of some of the pores by the deposited Ni metal. The values of S_{BET} and S_t were generally close in most of the samples, which indicated the presence of mesopores.

3.3. Optical characterisation

The UV–vis diffuse reflectance spectra of the parent $ZnSn(OH)_6$ and $Ni/ZnSn(OH)_6$ nanoparticles are displayed in Fig. 4. Compared to a measured wavelength of approximately 359 nm for the parent $ZnSn(OH)_6$ sample, the loading of Ni ions onto the $ZnSn(OH)_6$ caused a red shift to a value between 386 nm and 448 nm for different Ni loadings. The direct band gap energies for the parent $ZnSn(OH)_6$ and $Ni/ZnSn(OH)_6$ were calculated from their reflection spectra based on the method suggested by Mohamed [18], and the results are displayed in Table 2. It is clear that the energy gap decreased with an increase in the Ni ions. The band gap values were 3.45, 3.21, 3.03, 2.79 and 2.77 eV for $ZnSn(OH)_6$, 0.1 wt% $Ni/ZnSn(OH)_6$, 0.2 wt% $Ni/ZnSn(OH)_6$, 0.3 wt% $Ni/ZnSn(OH)_6$ and 0.4 wt% $Ni/ZnSn(OH)_6$, respectively. Photoluminescence (Pl) emission spectra have been used to study the transfer of photogenerated electrons and holes as well as to gain an understanding of the separation and recombination of photogenerated charge carriers. To investigate the photoelectric properties of the prepared samples, Pl spectra were obtained for the different samples, which were excited at 265 nm at room temperature, and the spectra are shown in Fig. 5. It is clear that the Pl intensity greatly decreased when the wt% of Ni was increased. Ni acts as a trapping site, which captures photogenerated electrons from the conduction band, thus separating the photogenerated electron/hole pairs. It is generally accepted that the incorporation of noble metal nanoparticles into semiconductor-based catalysts enhances the light absorption of the catalysts in the visible light region. This effect leads to a shift in the absorption edge towards longer wavelengths, which indicates a decrease in the band gap energy. Additionally, this effect leads to more photogenerated electrons and holes that are able to participate in the photocatalytic reactions. When using Ni as the noble metal, the interface of the $ZnSn(OH)_6$ is modified in a way that alters the mechanism by which photogenerated charge carriers undergo both recombination and surface reactions. This change would force $ZnSn(OH)_6$ to be more easily activated in the visible region. The shift in emission position can be attributed to the charge transfer between the Ni generated band and the semiconductor conduction band of $ZnSn(OH)_6$.

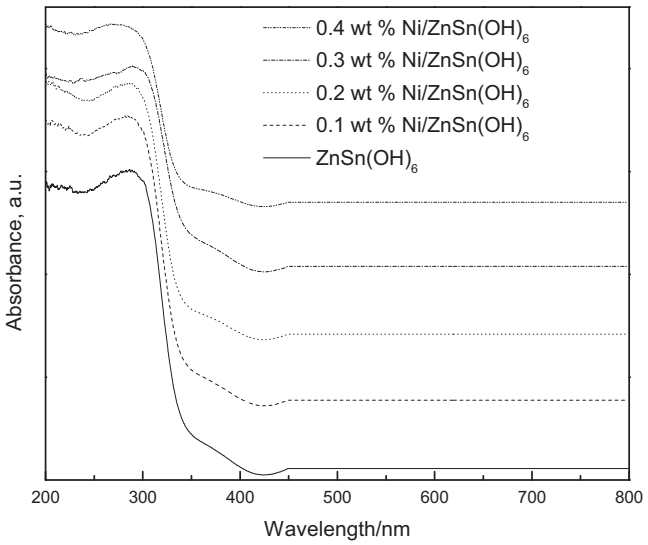

Fig. 4. UV–vis absorption spectra of $ZnSn(OH)_6$ and $Ni/ZnSn(OH)_6$ nanoparticles.

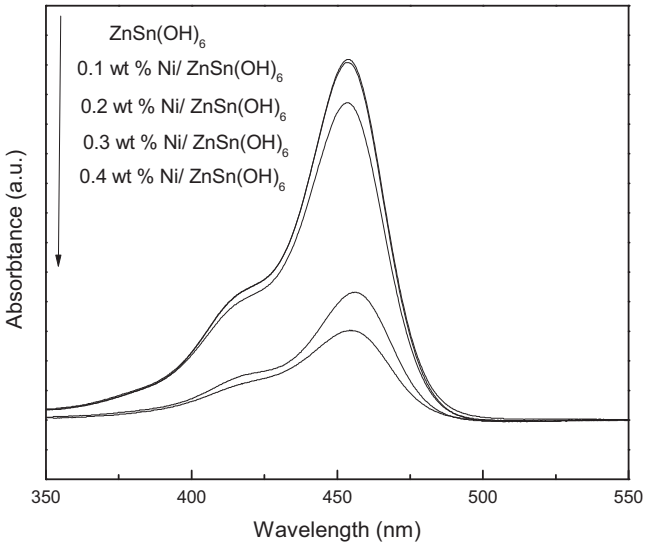

Fig. 5. Pl spectra of $ZnSn(OH)_6$ and $Ni/ZnSn(OH)_6$ nanoparticles.

3.4. Photocatalytic activity

3.4.1. Photocatalytic reduction of 4-nitroaniline

The photocatalytic activities of the prepared samples were studied by the photocatalytic production of PPD via 4-NA reduction under visible light irradiation. No 4-NA or PPD was detected in the absence of either the catalyst or light irradiation. Fig. 6 shows the photocatalytic reduction of 4-NA by both $ZnSn(OH)_6$ and $Ni/ZnSn(OH)_6$ samples under visible light. These

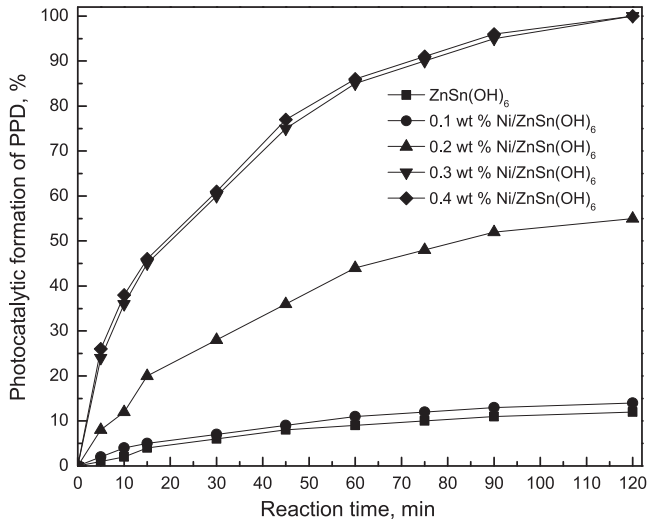

Fig. 6. Effect of the different catalysts for the photocatalytic reduction of 4-NA under visible light irradiation.

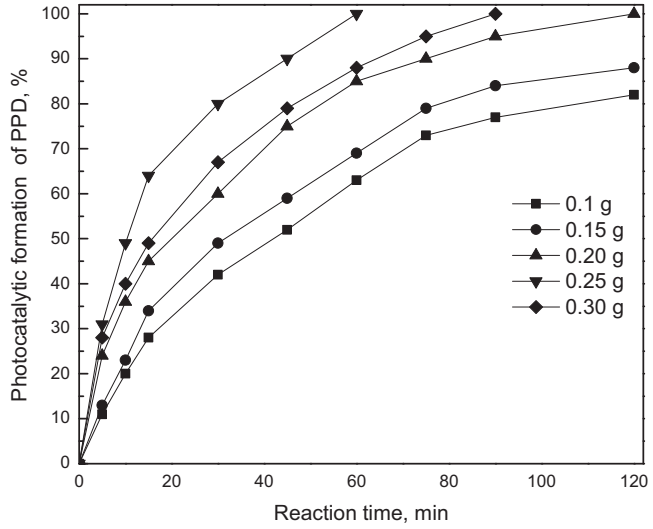

Fig. 7. Effect of the loading of 0.3 wt% Ni/ZnSn(OH)$_6$ on the photocatalytic reduction of 4-NA.

experiments were carried out under the following conditions: 40 ppm 4-NA, 80 mL of 4-NA/CH_3OH solution (1/99, v/v), and 0.2 g of catalyst. The results indicated that the photocatalytic activity increased in the following order: ZnSn(OH)$_6$ < 0.1 wt% Ni/ZnSn(OH) < 0.2 wt% Ni/ZnSn(OH) < 0.3 wt% Ni/ZnSn(OH) ≤ 0.4 wt% wt% Ni/ZnSn(OH). Therefore, the photocatalytic activity of the Ni/ZnSn(OH)$_6$ was dependent upon the Ni content. The photocatalytic activity increased as the Ni loading increased from 0.1% to 0.3%. Beyond 0.3%, the photocatalytic activity almost remains unchanged. Therefore, in this case, Ni loading sites acted as surface recombination centres for electron/hole pairs and, accordingly, suppressed the photocatalytic activity.

3.4.2. Effect of the amount of the photocatalyst on the photocatalytic reduction of 4-NA

The amount of photocatalyst used in the reaction was another important parameter of the photocatalytic reduction of 4-NA by visible light irradiation. Amounts of 0.3 wt% Ni/ZnSn(OH)$_6$ ranging from 0.1 to 0.3 g were added to 40 ppm of 4-NA. As shown in Fig. 7, the photocatalytic reduction of 4-NA increased when the amount of catalyst increased from 0.1 g to 0.25 g. However, a further increase in the amount of the photocatalyst above 0.25 g was less effective in the photocatalytic reduction reaction. An increase in the amount of the photocatalyst increased the number of active sites on the photocatalyst. Consequently, the numbers of 4-NA molecules and photons absorbed increased. However, at photocatalyst dosages above 0.25 g, the photocatalytic efficiency decreased as a result of the blockage of light penetration by the excessive amount of photocatalyst.

3.4.3. Photochemical stability

For practical applications of a photocatalyst, two factors related to recycling should be considered: the ease of separating the catalyst from solution and the stability of the catalyst, including retaining a high activity and resisting photocorrosion, after long-term usage. Therefore, the 0.3 wt% Ni/ZnSn(OH)$_6$ sample was selected to be reused five times to test its stability. After five catalysis cycles for the reduction of 4-NA, the 0.3 wt% Ni/ZnSn(OH)$_6$ sample did not show dramatic deactivation. The experimental data of XPS on the 0.3 wt% Ni/ZnSn(OH)$_6$ before and after reaction were shown in Fig. 2. The ratio of all peaks and their positions were nearly the same, which demonstrated that the as-prepared photocatalyst was stable in the photocatalytic process.

4. Conclusions

In summary, a Ni/ZnSn(OH)$_6$ photocatalyst was successfully synthesised and proved to be a promising catalyst due to its high photocatalytic efficiency with visible light promotion. A red shift phenomenon was found to increase as the wt% of the Ni doped onto the ZnSn(OH)$_6$ increased; this effect has been observed in the UV–vis spectra of ZnSn(OH)$_6$ and Ni/ZnSn(OH)$_6$ samples. Photocatalytic measurements of the photocatalytic reduction of a nitroaniline solution showed that ZnSn(OH)$_6$ nanoparticles with 0.3 wt% of Ni exhibited the highest catalytic activities and the most efficient photocatalytic properties for the reduction of nitroanoline, and these results may allow this material to find potential applications in related fields. The optimisation of reaction conditions led to the conclusion that 0.3 wt% Ni/ZnSn(OH)$_6$ with the use of 0.25 g of the catalyst in 80 mL of an 80 ppm solution of 4-NA yielded 100% conversion of 4-NA to PPD within 60 min of visible light irradiation. The experiments concerning reusing the catalyst revealed that the photocatalyst remained effective and active after five cycles, which indicated a promising recyclability of the Ni/ZnSn(OH)$_6$ photocatalyst.

References

[1] T. Clausen, A. Schwan-Jonczyk, G. Lang, W. Schuh, K.D. Liebscher, C. Springob, M. Franzke, W. Balzer, S. Imhoff, G. Maresch, R. Bimczok, Hair Preparations, John Wiley & Sons, Inc., New York, 2006.
[2] H. Engels, H. Weidenhaupt, M. Pieroth, W. Hofmann, K. Menting, T. Mergenhagen, R. Schmoll, S. Uhrlandt, Rubber, 4. Chemicals and Additives, John Wiley & Sons, Inc., New York, 2004.
[3] R.A. Smiley, Phenylene and Toluenediamines, John Wiley & Sons, Inc., New York, 2000.
[4] F.A. Harraz, O.E. Abdel-Salam, A.A. Mostafa, R.M. Mohamed, M. Hanafy, J. Alloys Compd. 551 (2013) 1.
[5] Y. Zhang, J. Wan, Y. Ke, J. Hazard. Mater. 177 (2010) 750.
[6] G. Tian, H. Fu, L. Jing, C. Tian, J. Hazard. Mater. 161 (2009) 1122.
[7] S. Sreekantan, L.C. Wei, J. Alloys Compd. 490 (2010) 436.
[8] A.M. El-Toni, S. Yin, T. Sato, T. Ghannam, M. Al-Hoshan, M. Al-Salhi, J. Alloys Compd. 508 (2010) L1.
[9] L.F. Velasco, J.B. Parra, C.O. Ania, Appl. Surf. Sci. 256 (2010) 5254.
[10] A.R. Khataee, M. Fathinia, S. Aber, M. Zarei, J. Hazard. Mater. 181 (2010) 886.
[11] H.F. Yu, S.T. Yang, J. Alloys Compd. 492 (2010) 695.
[12] K. Naeem, F. Ouyang, Physica B 405 (2010) 221.
[13] E. Rossetto, D.I. Petkowicz, J.H.Z. dos Santos, S.B.C. Pergher, F.G. Penha, Appl. Clay Sci. 48 (2010) 602.
[14] R.M. Mohamed, E.S. Baeissa, J. Alloys Compd. 558 (2013) 68.

[15] R.M. Mohamed, Desalin. Water Treat. 50 (2012) 147.
[16] W. Shu, Y. Liu, Z. Peng, K. Chen, C. Zhang, W. Chen, J. Alloys Compd. 563 (2013) 229.
[17] H. Yan, S.T. Kochuveedu, L.N. Quan, S.S. Lee, D.H. Kim, J. Alloys Compd. 560 (2013) 20.
[18] Y. Cao, Z. Zhao, J. Yi, C. Ma, D. Zhou, R. Wang, C. Li, J. Qiu, J. Alloys Compd. 554 (2013) 12.
[19] R.M. Mohamed, E.S. Aazam, Chin. J. Catal. 33 (2012) 247.
[20] R.M. Mohamed, E.S. Aazam, J. Alloys Compd. 509 (2011) 10132.
[21] R.M. Mohamed, E.S. Aazam, Int. J. Photoenergy 2011 (2011), Article ID 137328, 7 pp.
[22] R.M. Mohamed, I.A. Mkhalid, J. Alloys Compd. 501 (2010) 301.
[23] K. Chen, X. Feng, R. Hu, Y. Li, K. Xie, Y. Li, H. Gu, J. Alloys Compd. 554 (2013) 72.
[24] R.M. Mohamed, I.A. Mkhalid, J. Alloys Compd. 501 (2010) 143.
[25] R.M. Mohamed, K. Mori, H. Yamashita, Int. J. Nanopart. 2 (2009) 533.
[26] N. Castillo, R. Pérez, M.J. Martínez-Ortiz, L. Díaz-Barriga, L. García, A. Conde-Gallardo, J. Alloys Compd. 495 (2010) 453.
[27] M.Y. Abdelaal, R.M. Mohamed, J. Alloys Compd. 576 (2013) 201.
[28] Z.H. Li, Z.P. Xie, Y.F. Zhang, L. Wu, X.X. Wang, X.Z. Fu, J. Phys. Chem. C 111 (2007) 18348.
[29] T.J. Yan, X.X. Wang, J.L. Long, P. Liu, X.L. Fu, G.Y. Zhang, X.Z. Fu, J. Colloid Interface Sci. 325 (2008) 425.
[30] S. Meng, D. Li, M. Sun, W. Li, J. Wang, J. Chen, X. Fu, G. Xiao, Catal. Commun. 12 (2011) 972.
[31] H. Xue, Z.H. Li, L. Wu, Z.X. Ding, X.X. Wang, X.Z. Fu, J. Phys. Chem. C 112 (2008) 5850.